INT. J. REMOTE SENSING, 20 DECEMBER, 2003,
VOL. 24, NO. 24, 5243–5264

Taylor & Francis
Taylor & Francis Group

Radar stereo- and interferometry-derived digital elevation models: comparison and combination using Radarsat and ERS-2 imagery

M. GELAUTZ†*, P. PAILLOU‡, C. W. CHEN† and H. A. ZEBKER†

†Department of Electrical Engineering, Stanford University, Stanford, California 94305-9515, USA
‡Observatoire Astronomique de Bordeaux, BP 89, 33270 Floirac, France

(*Received 9 June 2000; in final form 7 February 2003*)

Abstract. In this experiment, we derive and compare radar stereo and interferometric digital elevation models (DEMs) of a study site in Djibouti, East Africa. A Radarsat stereo pair, as well as Radarsat and ERS-2 interferometric data, comprise the test images. The primary objective of the study was to analyse and compare the results obtained by the two techniques and explore possible synergisms between them. We find that in regions of high coherence, the DEMs produced by interferometry are of much better quality than the stereo result. However, the corresponding error histograms also show some pronounced errors due to decorrelation and phase-unwrapping problems on forested mountain slopes. On the other hand, the more robust stereo reconstruction, with an error standard deviation of 45 m, is able to capture the general terrain shape, although finer surface details are lost. In the second part of our experiment, we demonstrate that merging the stereoscopic and interferometric DEMs by applying a user-defined weighting function to a filtered coherence map can significantly improve the accuracy of the computed elevation maps.

1. Introduction

Over the past two decades, radar stereogrammetry and interferometry have evolved as two of the different approaches for generating digital elevation models (DEMs) from radar images. The two techniques present alternatives to conventional optical stereo mapping, which fundamentally depends on appropriate weather and illumination conditions and thus could exclude certain regions of the Earth temporarily—and, in some cases, even permanently—from successful observation. In the following, we start with a brief overview of radar stereo and interferometry (§1.1 and 1.2) and then discuss the objectives of our study in §1.3. For a more complete review of the related radargrammetric and interferometric

*Present address: Institute for Software Technology and Interactive Systems, Vienna University of Technology, Favoritenstrasse 9-11/188/2, A-1040 Vienna, Austria; e-mail: gelautz@ifs.tuwien.ac.at.

International Journal of Remote Sensing
ISSN 0143-1161 print/ISSN 1366-5901 online © 2003 Taylor & Francis Ltd
http://www.tandf.co.uk/journals
DOI: 10.1080/0143116031000115139

literature, the reader is referred to Toutin and Gray (2000) or Henderson and Lewis (1998).

1.1. *Stereo radargrammetry*

Of the two radar methods, stereo analysis—also known as stereo radargrammetry—was the first approach developed for extracting height information from Synthetic Aperture Radar (SAR) imagery. Following early work in the 1960s (La Prade 1963), more systematic research with real and simulated data began some 20 years later, stimulated by the growing availability of airborne and space-borne SAR scenes (Kaupp *et al.* 1983, Leberl *et al.* 1986). One major goal of those studies was to better understand the extent to which the principles and methods of conventional optical stereo analysis could be applied successfully to radar imagery. Leberl (1990) discussed the fundamentals of radar stereo mapping and presented related practical applications. Recent research carried out at the Canada Centre for Remote Sensing (Toutin 1997, 2000) focused on the accuracy of stereo-derived DEMs as a function of the observational geometry and local topography; in a Radarsat experiment with various look-angle combinations, elevation errors (90% confidence level) were found to range typically between 11 and 50 m in areas of low to moderate relief with automatic matching (Toutin 1999).

The ERS-1 satellite provided the main source of SAR data to the scientific community before 1995, when Canada's Radarsat satellite started its routine acquisition of SAR scenes with look angles varying between 10° and 60°. The fixed look angle of the ERS-1 sensor limited stereo applications to a roll–tilt experiment with incidence angles of 23° and 35° (Chen and Dowman 1996) and investigations with ascending/descending pairs (Toutin 1996). Very few reported efforts have utilized the relatively small look angle difference between overlapping parts of adjacent tracks for stereoscopic analysis, due to the insufficient stereo intersection angle. An example of a related study with ERS-1 data was published by Raggam *et al.* (1993). The same research group also performed a similar experiment with JERS-1 images (Raggam and Almer 1996). In the future, more stereo data will become available with the multi-incidence angle capability of the European Space Agency's (ESA's) Envisat satellite, which was launched in March 2002, and the Radarsat-2 mission planned for 2004.

A key step in stereo processing is stereo matching, i.e. the identification of corresponding points between the stereo partners. In many cases, matching errors constitute the most significant source of height errors in the reconstructed DEM. Stereo matchers typically encounter problems in areas with no significant topographic or thematic variation, because such areas do not provide significant texture for the unambiguous determination of corresponding points. Another source of matching errors are variations in image brightness, e.g. due to season-related changes such as temporal snow cover or freezing/thawing processes. The search for suitable automated matching techniques is an important topic in ongoing stereo research (Gülch 1991, Leberl *et al.* 1994, Dowman and Chen 1998).

1.2. *Interferometry*

After some early interferometric experiments (Rogers and Ingalls 1969, Graham 1974), research in SAR interferometry (InSAR) started to gain widespread interest

in the mid 1980s (Zebker and Goldstein 1986). Various studies (Prati and Rocca 1990, Zebker *et al.* 1992, Lin *et al.* 1994) have discussed and demonstrated the potential of the interferometric technique to produce high-resolution topographic maps with relative height errors of 5 m or less, as, for example, found by Zebker *et al.* (1994) in tests with 3-day repeat-pass ERS-1 imagery in relatively flat terrain. An example of the interferometric capabilities of the Radarsat sensor is described by Bamler *et al.* (1999). The authors report the generation of the first interferogram derived from the Radarsat ScanSAR mode as well as the combination of a conventional strip-map image with ScanSAR data for interferogram formation.

The potential of interferometry to provide a powerful tool for high-quality global topographic mapping led to the implementation of NASA's Shuttle Radar Topography Mission (SRTM 2000). During 11 days in February 2000, interferometric data were collected in a dual-antenna configuration over most parts of the Earth's land surface between 60° N and 56° S. Efforts now concentrate on processing this unique dataset to form consistent elevation maps with nearly worldwide coverage that includes regions where little or no topographic data had been available before.

However, the interferometric method also has several drawbacks and limitations. In repeat-pass systems, temporal decorrelation limits the applicability of the technique to those regions where surface properties remain sufficiently stable between the two SAR acquisitions. Even in single-pass configurations, baseline decorrelation and phase-unwrapping problems—that is, errors in resolving the 2π phase ambiguities—can seriously affect the accuracy of the estimated heights (Massonet and Rabaute 1993). One major problem when trying to resolve the phase ambiguities remains the proper recognition of those locations where surface discontinuities or undersampling of the terrain cause neighbouring phase values to differ by more than π rad. Furthermore, phase-unwrapping algorithms that aim to provide global coverage must fill in areas of low coherence (e.g. caused by vegetation) with reasonable estimates of the unwrapped phase, while at the same time errors arising in the low-quality regions must be prevented from spreading into other parts of the image.

1.3. *Our objectives*

The main goal of our study is to compare the advantages and limitations of stereoscopic and interferometric terrain mapping in application to a common study area. Most related studies on DEM generation have employed either stereo or interferometry exclusively and therefore do not provide a direct comparison of the two techniques in application to one and the same test site. In our experiment, we use a same-side Radarsat stereo pair and a fully automatic matching algorithm to generate a DEM of a test site in Djibouti, East Africa. Radarsat and ERS-2 interferometric data of the same terrain are utilized for computing interferometry-derived DEMs. We analyse the quality of the stereo and interferometric results by comparing them to a reference DEM derived from optical-stereo SPOT observations. In order to evaluate the stereoscopic and interferometric elevation maps under various topographic conditions, we have chosen a study area which exhibits a variety of relief characteristics, including rather flat, uniform areas as well as mountainous regions and terrain discontinuities. The terrain comprises arid desert regions as well as sections covered with vegetation. Thus, the scene contains

features which are expected to strain both the stereo matching and the interferometric phase-unwrapping algorithms.

In the second part of our experiment, we address the question of whether it is possible to combine the two techniques in such a way that one method helps overcome the deficiencies of the other. Due to the growing number of Earth-observing satellites, the development of techniques that combine height data obtained from different sources has become a topic of increasing importance. However, practically no literature is currently available on the merging of radar stereo and interferometric techniques to produce DEMs. This can partly be explained by the limited amount of spaceborne stereo imagery that was available before the launch of the Radarsat satellite in 1995. In our fusion experiment in §5, we first assess the utility of the interferometric coherence as an indicator of the quality of the InSAR heights and then suggest a fusion algorithm which merges the stereo and interferometric DEMs using coherence-derived weights.

In the following section of this paper, we give a brief comparison of the stereoscopic and interferometric techniques from a theoretical point of view. We discuss some aspects of the DEM generation process which are of particular interest for the identification of analogies, differences, and possible synergisms between the two techniques. Then, in §3, we demonstrate the stereo (§3.2) and InSAR (§3.3) techniques by using Radarsat and ERS-2 images of the Djibouti test site to form DEMs. The results obtained by the two techniques are evaluated and compared in §4. Finally, §5 presents the fusion experiment and illustrates the achieved improvements.

2. Stereo and InSAR geometry: theory

The principles of applying radar interferometry and stereogrammetry for DEM generation can be found in, for example, Zebker *et al.* (1994) and Leberl (1990). Figure 1 shows the basic geometry of the interferometric and stereoscopic image acquisitions. From the geometric point of view, an interferometric image pair can be regarded as a stereo pair with a very small intersection angle (or baseline). However, it should be noted that viewing angle differences usable for same-side stereo analysis typically range from around 5° to 45° and are thus on a different order of magnitude than the usable viewing angle differences of interferometric pairs. As an example, a critical interferometric baseline of 1 km at a satellite altitude of 800 km yields an intersection angle of less than 0.1°.

For the sake of clarity, the sketch in figure 1 utilizes simplifying assumptions such as a flat-Earth approximation and parallel flight paths with the same altitude. We suppressed additional details that are not necessary for understanding the principal geometric analogies and differences between the two techniques, as discussed in this section, in order not to overload the illustration. However, it should be noted that these simplifying assumptions were not used during the actual data processing described later in this paper and have therefore no impact on the results obtained in §3–5. In figure 1, the relative height of the target T above the reference plane is denoted Δh. The sensor positions S_1 and S_2 form a stereo pair with corresponding look angles θ_1 and θ_2. Their interaction with the local topography leads to the terrain-induced stereo parallax Δp. The relationship

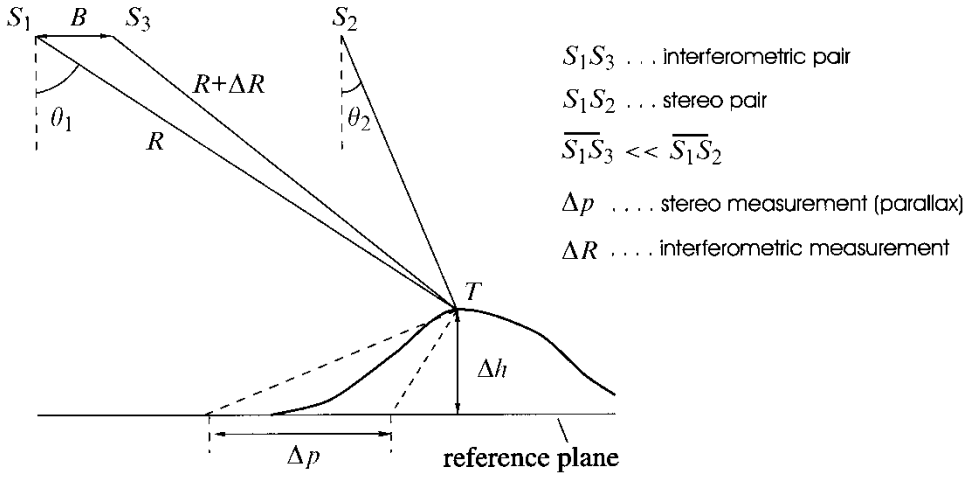

Figure 1. Stereoscopic and interferometric imaging geometry. The principal relationships between terrain height Δh and the stereo and interferometric measurements Δp and ΔR, respectively, are sketched. The symbols used are explained in more detail in the text.

between the stereoscopic measurement Δp and the elevation Δh is given by

$$\Delta p \approx (\cot\theta_2 - \cot\theta_1)\cdot\Delta h \tag{1}$$

Relationship (1) can also be written as

$$\Delta p \approx \left(\frac{\tan\theta_1}{\tan\theta_2} - 1\right)\cdot\cot\theta_1\cdot\Delta h \tag{2}$$

The interferometric image pair is captured from sensor positions S_1 and S_3, which are separated by the baseline B. The distance between S_1 and the location T on the ground corresponds to the slant range R. We can relate the phase difference $\Delta\Phi$, measured in the interferogram, to the slant range offset ΔR (see figure 1) according to

$$\Delta\Phi = -\left(\frac{4\pi}{\lambda}\right)\cdot\Delta R \tag{3}$$

where λ denotes the radar wavelength. Following the formulae used by Sansosti *et al.* (1999) for the approximate relationship between the observed interferometric phase $\Delta\Phi$ and the topographic term Δh, and under the additional simplifying assumption of a horizontal baseline, we obtain

$$\Delta\Phi - \Phi_0 \approx \left(\frac{4\pi}{\lambda}\right)\cdot\left(\frac{B}{R}\right)\cdot\cot\theta_1\cdot\Delta h \tag{4}$$

or

$$\Delta R - R_0 \approx B/R\cdot\cot\theta_1\cdot\Delta h \tag{5}$$

The value Φ_0 (R_0) denotes a phase (range) offset which depends on the parallel component of the interferometric baseline. Comparison of (2) and (5) shows the similar structure of the stereo and interferometric relationships, which can both be

described by

$$\Delta x \approx K \cdot \cot \theta_1 \cdot \Delta h \tag{6}$$

In the stereo case, Δx and K correspond to

$$\Delta x = \Delta p \tag{7}$$

$$K = \left(\frac{\tan \theta_1}{\tan \theta_2} - 1 \right) \tag{8}$$

In the interferometry case, the corresponding relationships are

$$\Delta x = \Delta R - R_0 \tag{9}$$

$$K = B/R \tag{10}$$

If we substitute the look angles $\theta_1 = 37^\circ$ and $\theta_2 = 28^\circ$ of our Radarsat stereo pair (see table 1) in equation (8), we obtain $K = 0.42$. If we assume an interferometric imaging geometry with values of $B = 400\,\text{m}$ and $R = 800\,\text{km}$, equation (10) delivers $K = 0.0005$. The different values of K reflect the fundamental difference in magnitude between the stereoscopic measurement Δp in (7), which is on the order of the pixel size (i.e. several metres), and the interferometric range measurement ΔR from (9), which is on the order of the radar wavelength, which is typically several centimetres.

In the following, we often use the term baseline to denote either the interferometric baseline B or the stereo intersection angle (θ_2–θ_1). In both stereo and interferometry, the sensitivity to system noise in the parallax/phase measurement increases as the baseline decreases. Larger baselines improve the height resolution, but at the same time, increasing baselines or look angle differences are associated with geometric dissimilarities between the two images at the wavelength and pixel levels. This leads to interferometric baseline decorrelation as well as more pronounced geometric and radiometric differences between the stereo partners, which make the matching process (i.e. the parallax detection) more difficult. In addition, longer interferometric baselines introduce more numerous phase ambiguities and, hence, phase-unwrapping difficulties. Generally, the selection of an optimal stereoscopic or interferometric viewing geometry for a given application must be based on a compromise between these competing effects, with the due consideration given to the local topography and scene content.

In a practical application, uncertainties in the sensor position can lead to significant errors in both the stereo- and interferometry-derived height maps. The

Table 1. Overview of stereo and interferometric data.

	Stereo	Interferometry	
Sensor	Radarsat std2/4	Radarsat std4	ERS-2
Orbit	desc.	desc.	asc.
Acquisition dates	09 Dec 1997 (std2) 26 Feb 1998 (std4)	26 Feb 1998 22 Mar 1998	31 Aug 1997 05 Oct 1997
Format	SLC	SLC	raw
Look angle (°)	28/37	37	23
Temporal baseline (days)	79	24	35
Ambiguity height (m)	–	54	17

correction of these systematic errors usually requires the use of ground control points (GCPs). The acquisition of a sufficient number of high-quality GCPs with an appropriate spatial distribution is often time-consuming, while the quality of the measurements depends on the experience of the human operator. Raggam and Almer (1990) proposed the use of least-squares techniques for GCP-based refinement of the stereo model and space intersection.

Chen and Dowman (2001) addressed recently the particular problem of sensor position errors in the along-track direction (e.g. azimuth timing errors) in the context of control point acquisition for stereo measurements. The authors developed a weighted least-squares algorithm that makes the radargrammetric model more robust to azimuth errors and show that the proposed method can significantly reduce the number of necessary ground control points and the requirements on their spatial distribution.

In interferometry, an important source of errors is uncertainty in the interferometric baseline. Zebker *et al.* (1994) show that it is impossible to distinguish an error in the baseline angle from a slope on the surface topography and report experiments with GCP-based baseline estimation. Despite ongoing efforts in high-precision orbit determination (Scharroo and Visser 1998), the acquisition of GCPs for orbit refinement still remains an important issue in many practical mapping tasks. In our experiment in §3, we employ GCPs to suppress geometric modelling errors as far as possible in order to concentrate the subsequent analysis on technique-related effects such as stereo matching or phase-unwrapping problems.

3. Stereoscopic and interferometric DEMs: experiments and results

3.1. *Test site and dataset*

Our study area is the Asal Rift, an arid volcanic region located in the Republic of Djibouti, East Africa. In order to provide topographic diversity, we have selected a test site that contains both relatively flat, homogeneous regions as well as areas of rough relief. Figure 2(*a*) shows the reference DEM with different terrain heights represented by different colours. The displayed terrain heights range from 180 to 1400 m. The DEM was derived from optical stereo analysis (see below) and has a spatial resolution of 75 m. The lower-lying terrain is mainly covered by basaltic sediments and exhibits some graben structures. The mountains in the northern part of the scene are partially forested.

For our stereo investigations, we employed a Radarsat pair, which was acquired in standard (std) 2 and 4 mode during a descending orbit with mean look angles of 28° and 37°, respectively. The interferometric dataset consists of a descending Radarsat image pair—the std4 stereo image with a corresponding interferometric partner—and an ascending ERS-2 image pair. Table 1 summarizes the characteristics of these data. The original data were resampled to a ground resolution of approximately 20 m in both dimensions. The interferometric ambiguity height listed in table 1 gives the difference in terrain elevation that corresponds to one cycle (2π rad) of interferometric phase. The Radarsat scenes were delivered in single look complex (SLC) format, whereas we processed the ERS raw data using our own SAR processor. The processor is a variant of the Repeat Orbit Interferometry Package (ROI_PAC), which was developed jointly by the Jet Propulsion Laboratory (JPL) and the California Institute of Technology (Buckley *et al.* 2000).

The reference DEM was generated from two SPOT Panchromatic scenes with

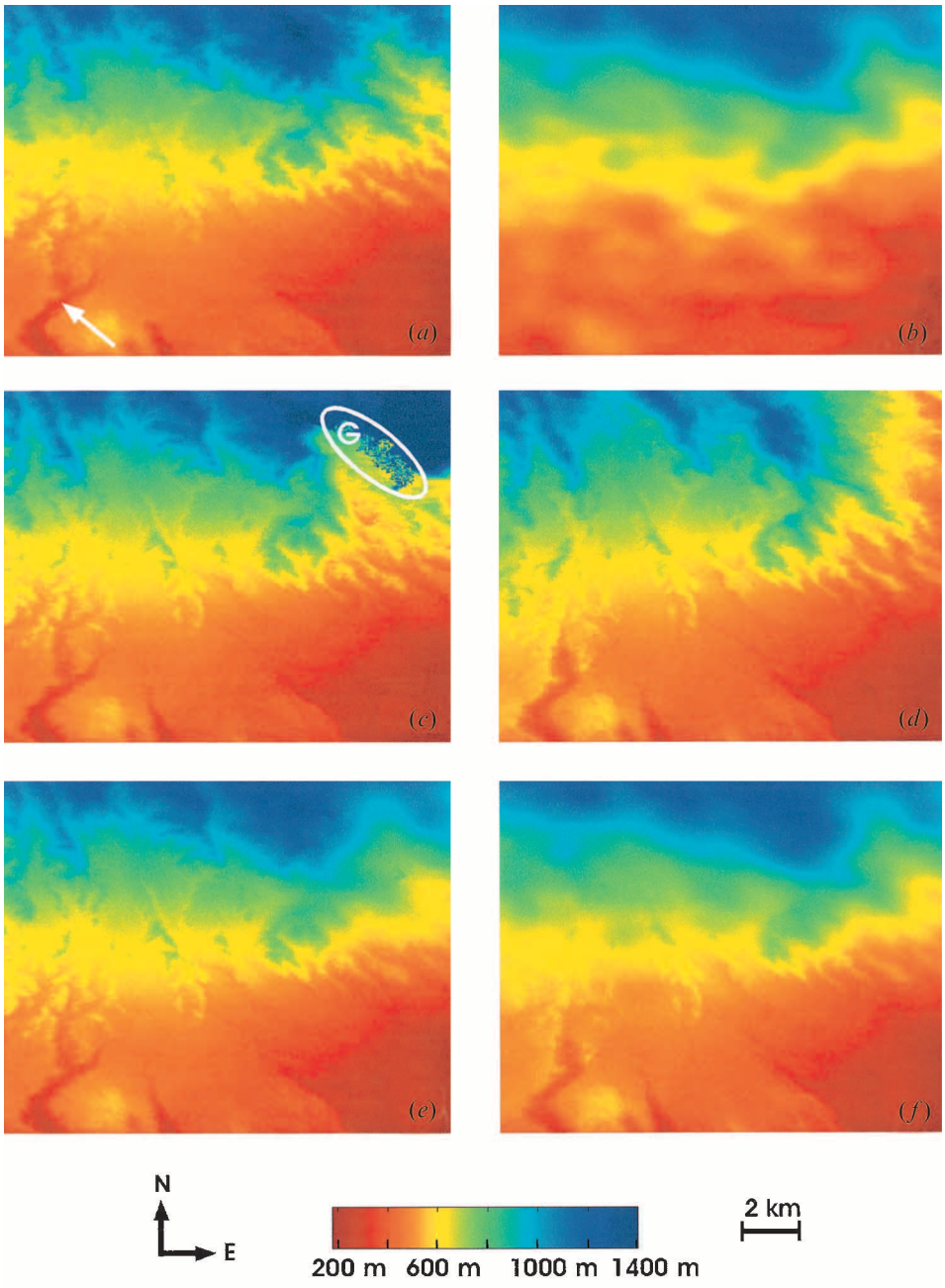

Figure 2. DEMs of the Asal Rift test site. The area shown covers approximately 11 km × 12 km, and elevations displayed vary between 180 and 1400 m. (*a*) SPOT reference DEM, (*b*) Radarsat stereo DEM, (*c*) Radarsat interferometric DEM, and (*d*) ERS-2 interferometric DEM. The bottom row shows the stereo–interferometry merged DEMs using Radarsat (*e*) and ERS-2 (*f*) interferograms. The arrow in (*a*) indicates a surface detail that is not visible in (*b*). In (*c*), some geocoding artefacts are visible within region G.

10 m pixel spacing using the Erdas Imagine software (OrthoBASE module). Topographic maps at a scale of 1 : 100 000 with contour line intervals of 25 m provided the GCPs. In order to estimate the difference between the topographic maps and the SPOT-derived DEM, we vectorized the topographic information from the maps and employed a kriging interpolation method with a Gaussian variogram model (Cressie 1991) to compute a difference DEM for several subregions presenting both low and high relief conditions. As a result, a maximum vertical height difference of 10 m was found.

In the ERS and Radarsat interferograms, one phase cycle corresponds to a height difference of 17 m and 54 m, respectively, while the pixel spacing in each of these interferograms is 20 m. Comparing these figures with the 10 m relative height error computed for the SPOT DEM and additionally taking into account errors in the topographic maps as well as possible interpolation errors, one can infer that in areas of high-quality interferometric results the SPOT DEM cannot be considered a reliable reference for the interferometric reconstruction. However, it is important to note that in our experiment we concentrate primarily on height errors on the order of several phase cycles; these can be easily identified with the use of the SPOT DEM. As we will show, only these pronounced elevation errors are relevant when merging interferometric and stereoscopic elevation maps to achieve more accurate height estimates.

3.2. *Stereo processing*

The starting point of our stereo experiment was the Radarsat image pair (see table 1) shown in figure 3(*a*) and (*b*). Because of the rather small stereo intersection angle of about 9°, the images in 3(*a*) and (*b*) appear quite similar. By substituting the look angles of 28° and 37° into equation (1) we find that for our imaging configuration a parallax error of one pixel, which corresponds to approximately 20 m on the ground, delivers a vertical height error of approximately 36 m.

After resampling the original SLC data, we pre-processed the images using a gradient filter that was specially designed to suppress speckle noise and enhance image structures due to relief (Paillou and Gelautz 1999). As a next step, we applied a hierarchical correlation-based algorithm developed by Frankot *et al.* (1994) for the matching and registration of noisy SAR imagery in order to automatically determine the parallaxes between the stereo partners. The algorithm first selects a regular reference grid in one of the images and then searches the second image for corresponding points at successively finer resolution levels. In our tests, we employed window sizes of 64, 32, 16 and 8 pixels to generate a final match point grid with a nominal spacing of 160 m. For each match point, a confidence value is computed from the 2D curvature of the corresponding correlation surface. Then, a threshold is applied to discard match points with low reliability, i.e. points which do not exhibit a pronounced peak in the correlation surface. A more detailed description of the algorithm can be found in Frankot *et al.* (1994).

We converted the match points to terrain height by computing the rigorous stereo solution, that is, the intersection of the two range/Doppler circles which are defined by corresponding points in the two stereo images (Leberl 1990). We used a set of 30 ground control points (GCPs) to improve the initial stereo model that was derived from the available orbit data. A well-discernible coast line—not visible in the section shown in figure 3—provided a good reference in several parts of the

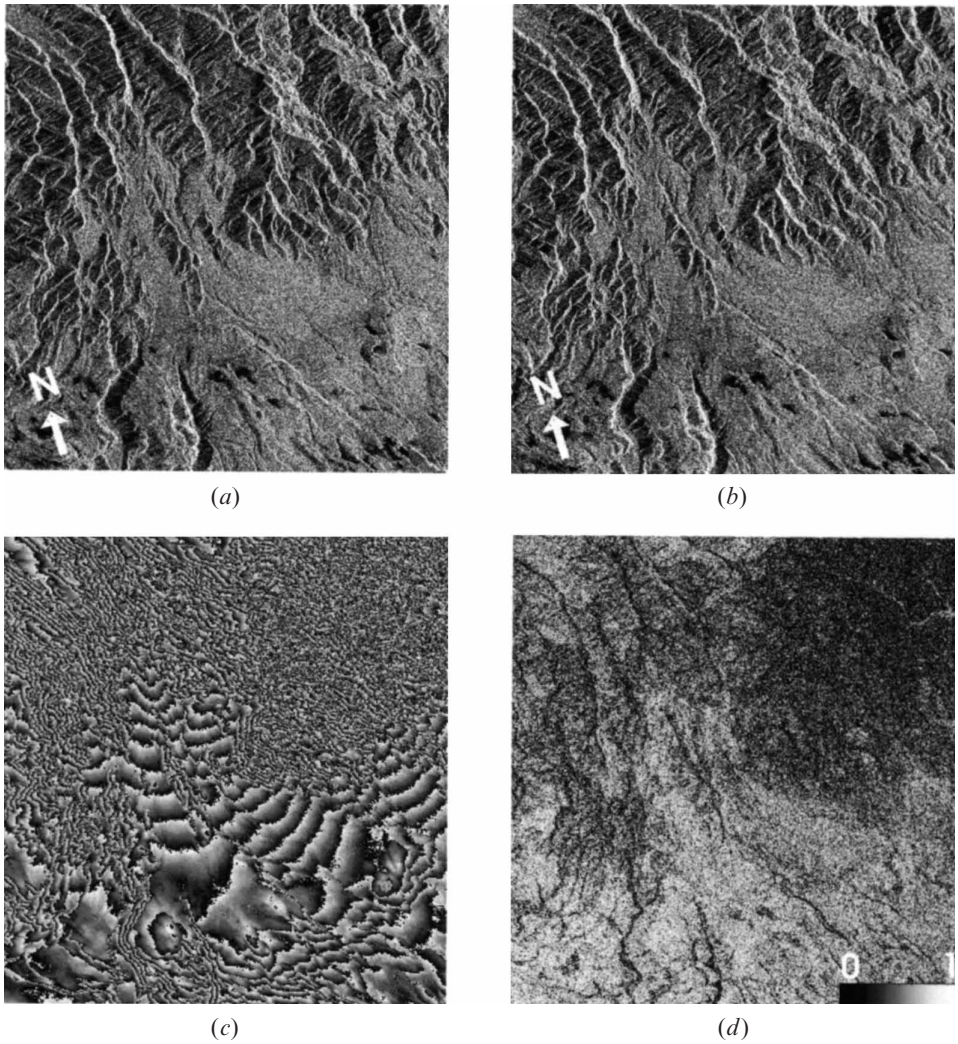

(*a*) (*b*)

(*c*) (*d*)

Figure 3. Radarsat stereo and interferometric dataset. The top row shows the std2/std4 stereo pair acquired with mean look angles of 28° (*a*) and 37° (*b*). The scenes were illuminated from the right and cover approximately 260 km^2. The bottom row gives the std4 interferogram (*c*) and the corresponding coherence map (*d*).

original SAR scenes. For some GCP measurements, we incorporated additional height information from our reference DEM in order to improve the accuracy of the 1 : 100 000 map readings. No separate check on the accuracy of the GCPs was performed. After DEM generation (see §4), we found a residual error with a mean of 6.4 m and a standard deviation of 45 m with respect to the reference DEM.

The parameter refinement and stereo intersection were performed using the RSG software of Joanneum Research (RSG 1993). The optimization of the imaging geometry resulted mainly in an adjustment of the values for offset and pixel spacing in both the range and azimuth direction.

The stereo-derived DEM can be seen in figure 2(*b*). Comparison with the SPOT

reference DEM in figure 2(*a*) shows that stereo was able to recover the main terrain structures (see, for example, the mountain ridges in the upper half of the DEM), whereas finer, high-frequency surface information is missing. This loss of topographic detail is particularly obvious in the relatively flat southern part of the DEM. For example, the lower-lying fork-shaped feature marked by an arrow in figure 2(*a*) cannot be recognized in the stereo DEM in figure 2(*b*). It should be noted that the ability of radar stereo to capture surface details normally cannot be refined arbitrarily by simply increasing the match point density. We carried out additional tests with match point postings located 4 pixels apart—instead of the 8-pixel grid used previously—and did not observe any significant changes of the results.

3.3. *Interferometric processing*

The flattened interferogram produced from the Radarsat std4 interferometric pair can be seen in figure 3(*c*). It was formed by averaging four pixels in azimuth and one pixel in range, resulting in a ground pixel spacing of approximately 20 m in both dimensions. One 2π phase cycle in the interferogram corresponds to a 54 m height difference. The coherence map shown in figure 3(*d*) was estimated by applying a 2×2 averaging mask. Lower coherence values are displayed as dark, according to the scale in the bottom right corner of the image. The rough topography in the upper part of the scene along with vegetation cover in the north-east leads to poor correlation, thus providing areas of dense residues during phase unwrapping.

We unwrapped the interferogram using the dynamic-cost cycle-cancelling (DCC) technique proposed by Chen and Zebker (2000). As opposed to the classic residue-cut method introduced by Goldstein *et al.* (1988), the DCC algorithm provides global coverage and allows the incorporation of user-defined weights. For topographic applications, meaningful weights are derived from edges in the amplitude image, which suggest the occurrence of terrain discontinuities.

For one of the Radarsat interferometric images, a refined imaging model was already available from the previous stereo analysis. During the geocoding of the unwrapped phase values, we employed five additional GCPs collected in our reference map to compensate for remaining baseline uncertainties. In §4, we will present the interferometric error histograms which show that the GCPs were of sufficient quality to suppress any significant baseline-induced slope on the surface topography.

A Delaunay triangulation with bilinear interpolation was used to fill in missing elevation data due to undersampling of the terrain in foreshortening and layover regions. The computed InSAR DEM as well as the SPOT reference DEM were resampled to a common reference grid of 37.5 m. We performed additional tests with other grid sizes (using, for example, the original 75 m postings of the SPOT DEM) as well as different interpolation algorithms such as Akima interpolation (Akima 1978), but the results of the subsequent error analysis remained basically unchanged.

The resulting interferometric DEM can be seen in figure 2(*c*). Visual comparison with the reference DEM in figure 2(*a*) shows a high-quality reconstruction in the unvegetated parts of the scene. However, pronounced height errors occur in the mountainous regions in the north-east. These reconstruction errors can be attributed mainly to decorrelation in forest land, which results in meaningless

phase values. Some geocoding artefacts that are visible inside the region G in the upper right corner of figure 2(*c*) are caused by erroneous elevation discontinuities introduced by the phase unwrapping.

Similarly, we processed the ascending ERS-2 interferometric data into an interferogram with an ambiguity height of 17 m. The ERS-2 interferometric dataset is shown in figure 4. The result obtained after projecting the unwrapped phase values into the geometry of the reference DEM is displayed in figure 2(*d*). As in the Radarsat case, the most severe height errors occurred in the top right corner of the scene.

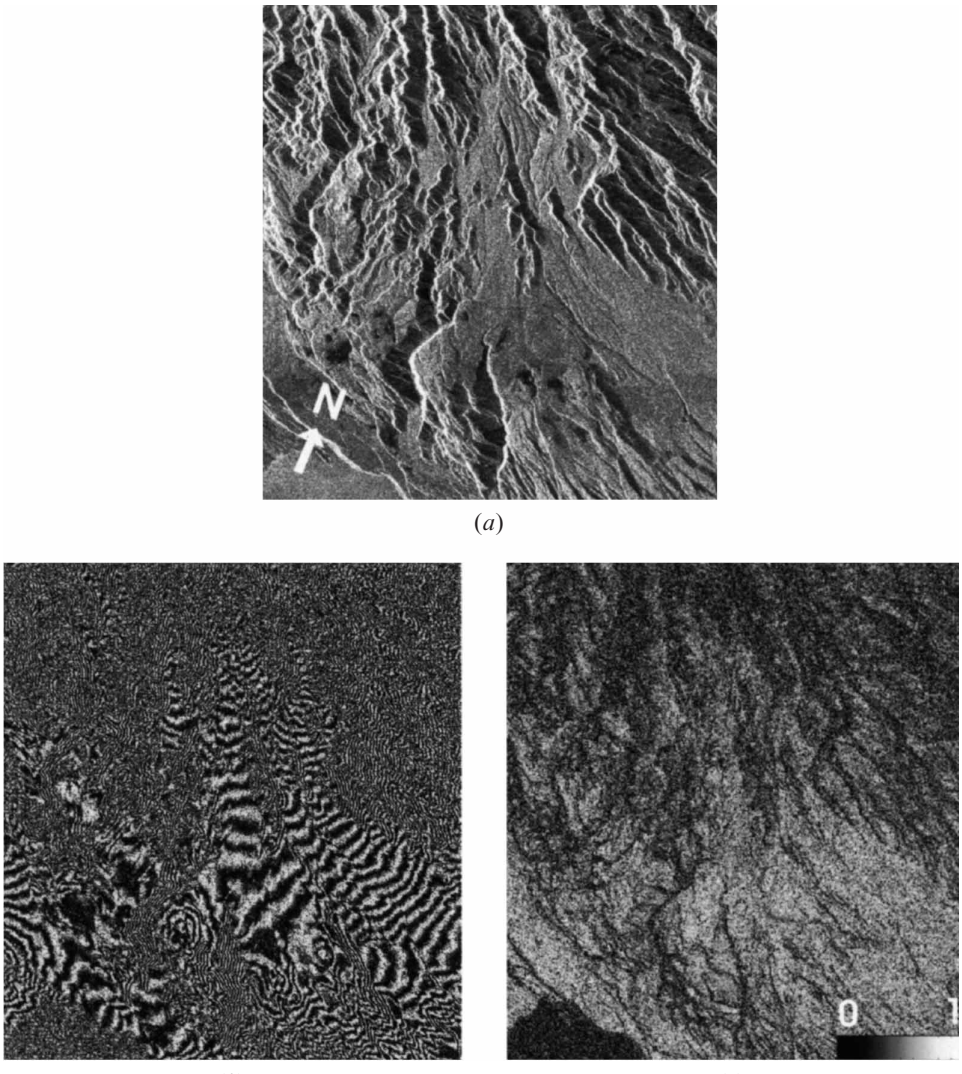

(*a*)

(*b*)

(*c*)

Figure 4. ERS-2 interferometric dataset: (*a*) magnitude image, (*b*) interferogram, and (*c*) coherence image. The scene was acquired from the left during an ascending orbit.

4. Comparison and accuracy analysis

The difference DEMs between the SPOT reference and the various reconstructed DEMs are shown in figure 5. In order to enhance visibility and

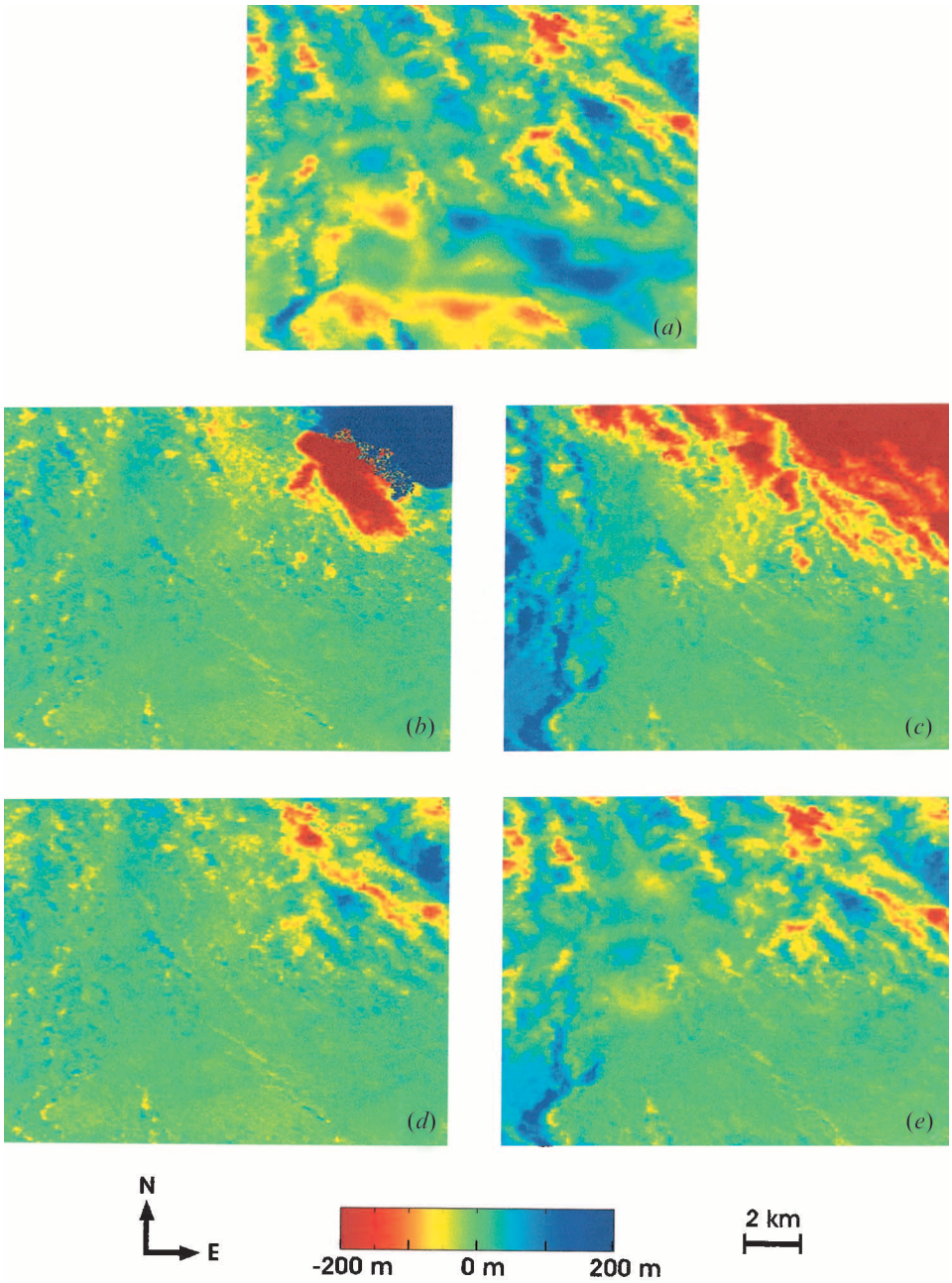

Figure 5. Difference DEMs with respect to SPOT reference DEM: (*a*) Radarsat stereo, (*b*) Radarsat interferometry, (*c*) ERS-2 interferometry, (*d*) Radarsat/Radarsat stereo–interferometry merged DEM, and (*e*) Radarsat/ERS-2 stereo–interferometry merged DEM.

Table 2. Distribution of reconstruction error.

DEM	Reconstruction error (%)					
	> 25 m	> 50 m	> 75 m	> 100 m	> 150 m	> 200 m
Stereo	56.7	26.0	10.1	3.5	0.2	0.0
InSAR (Radarsat)	24.4	12.6	10.2	9.3	8.0	6.9
Merged DEM (Radarsat)	21.6	6.9	3.0	1.2	0.1	0.0
InSAR (ERS-2)	47.1	33.4	25.8	18.7	10.7	6.8
Merged DEM (ERS-2)	34.8	14.4	5.5	2.1	0.2	0.0

facilitate comparison, the displayed height errors are limited to values between -200 and $+200$ m, although in some low-coherence regions the interferometric errors exceed this range. Table 2 gives a closer look at the distribution of the elevation errors. The table entries show that about 7% of the reconstructed interferometric height values exceed the ± 200 m error range. Occasionally, error values of up to approximately -600 m/$+1000$ m were found in the ERS-2/Radarsat interferogram, as we will show later in the scatter plots of §5 (figure 7).

When examining figure 5(*a*), we can see that the stereoscopic errors are distributed rather evenly throughout the whole scene. Some of the error patterns are directly related to high-frequency terrain structures that the stereo technique failed to detect. Other reconstruction errors, especially in the smoother sections of the test site, can be attributed for the most part to matching errors which do not follow the relief. In a quantitative analysis of the stereo DEM, we found a mean error and standard deviation of 6.4 m and 45 m, respectively, with respect to the SPOT DEM.

Contrary to the stereo case, the Radarsat and ERS-2 interferometric errors displayed in figure 5(*b*) and (*c*), respectively, are characterized by a patch-like spatial distribution arising from the phase-unwrapping process, which introduces integer-cycle jumps into the solution (Chen and Zebker 2000). One can recognize areas of high reconstruction precision (the greenish regions in figure 5(*b*) and (*c*)), where the interferometric DEM is of comparable quality as the SPOT DEM, along with patches of elevation errors—the bluish and reddish regions in figure 5(*b*) and (*c*)—which are mainly associated with decorrelation and phase-unwrapping problems. In addition to the severe underestimation of the terrain height in the north-eastern corner of the ERS-2 DEM, a zone of moderate errors with reconstruction inaccuracies on the order of approximately five phase cycles, or 85 m, is visible along the left border of figure 5(*c*). These errors on the west side of the ERS DEM, which apparently follow the local topography, do not appear in the Radarsat InSAR DEM in figure 5(*b*). They are probably a result of the steeper look angle of the ERS sensor, which increases the occurrence of layover and related phase-unwrapping errors.

The Radarsat stereo and ERS-2 interferometric error histograms corresponding to the difference DEMs in figure 5(*a*) and (*c*), which utilize the SPOT DEM as reference, are shown in figure 6(*a*). The two curves were centred around the mean value of the stereo curve. A small offset of the interferometric peak, which remained after GCP calibration can be considered non-significant; it does not affect our further analysis, which concentrates on the suppression of outliers in the histogram wings.

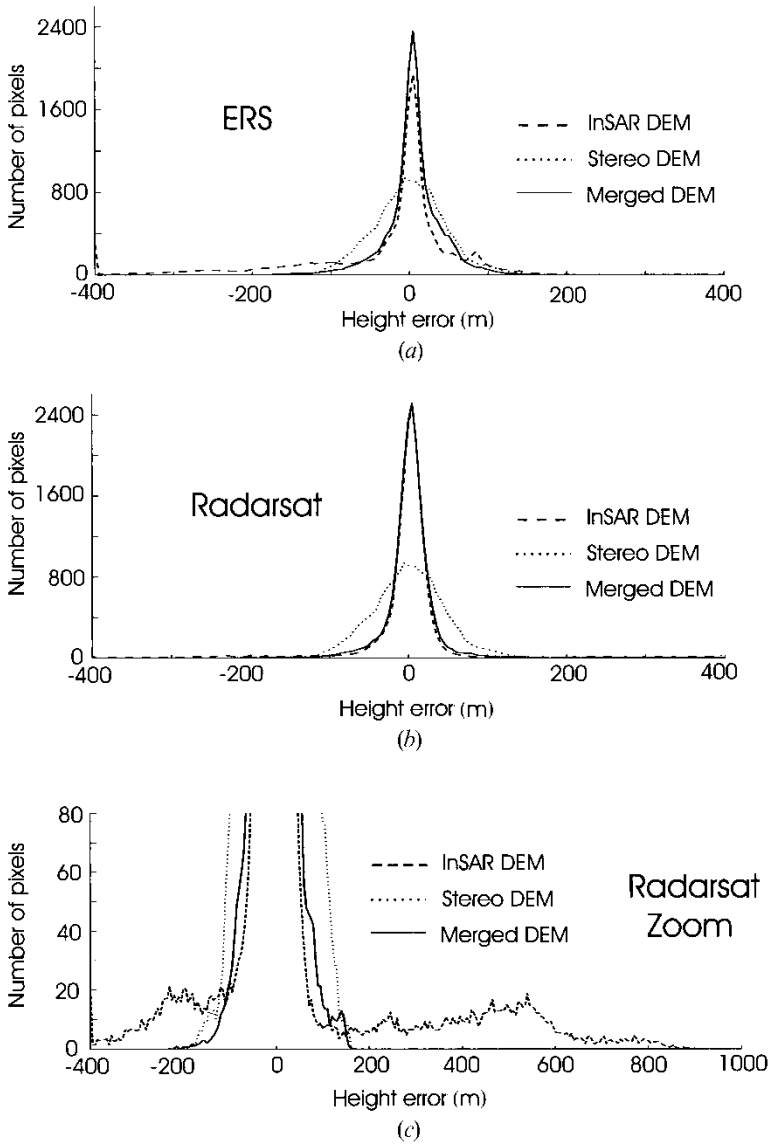

Figure 6. Error histograms before and after merging. (*a*) The error histograms corresponding to the difference DEMs shown in figure 5(*a*), (*c*) and (*e*). The histograms in (*b*) correspond to the difference DEMs in figure 5(*a*), (*b*) and (*d*). (*c*) An enlarged view of the histogram tails from (*b*).

The shapes of the histograms confirm that the stereo reconstruction (dotted curve) is less accurate but more robust than the interferometric reconstruction (dashed curve). The high quality of the interferometric result is reflected by the pronounced histogram peak. However, the interferometric DEM is corrupted by errors due to low coherence and phase-unwrapping problems, which account for points in the outer regions of the histogram. For example, the secondary peak at

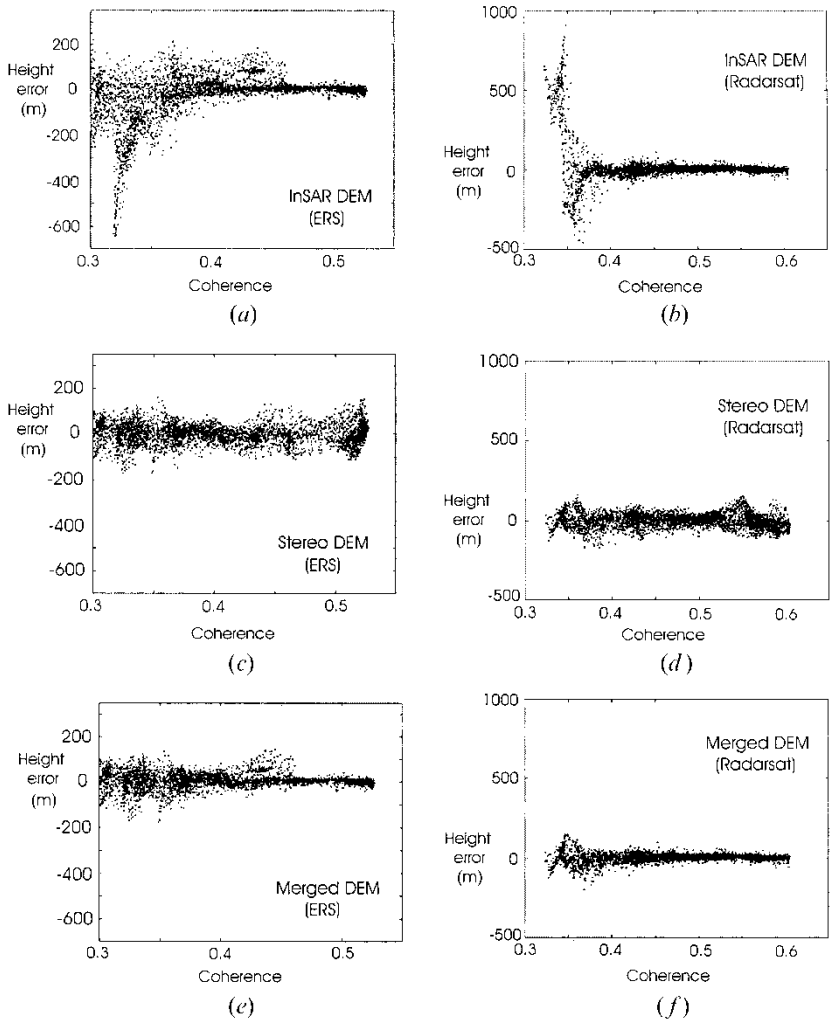

Figure 7. Height error versus interferometric coherence: (*a*) ERS-2 interferometry, (*b*) Radarsat interferometry, (*c*) Radarsat stereo (using ERS-2 coherence), (*d*) Radarsat stereo (using Radarsat coherence), (*e*) Radarsat/ERS-2 stereo–interferometry merging result, (*f*) Radarsat/Radarsat stereo–interferometry merging result.

values around 85 m corresponds to the moderate height errors visible at the left edge of figure 5(*c*). The non-zero values in the left histogram tail reflect the heavily corrupted area in the upper right corner of the DEM.

Figure 6(*b*) shows the error histogram of the Radarsat InSAR reconstruction (dashed curve) in comparison to the Radarsat stereo result (dotted curve). Similarly to the ERS case in figure 6(*a*), the Radarsat interferometric curve exhibits a much higher central peak than the stereo histogram. The interferometric errors in the outer regions of the histogram, which are not visible in figure 6(*b*), can be recognized in the enlarged view in figure 6(*c*).

5. Fusion experiment

The goal of our fusion experiment is to merge the stereo- and interferometry-derived height maps in such a way that the fusion DEM combines the good properties of each individual technique. As a first step, we investigated the utility of the interferometric coherence as an indicator of the quality of the InSAR DEMs. A low-pass filter was applied to the coherence image—which contains real values between 0 and 1—in order to suppress noise and minor local variations which were found not to carry useful information. This (real-value) low-pass filtering was carried out on top of the initial (complex-value) coherence estimation that was performed during earlier processing stages. Another possibility would have been to use a larger averaging window during the initial coherence estimation. In our experiment, however, we preferred the two-step implementation, because it better matches the structure of our SAR processing software; the coherence map obtained from the 2×2 filter (see §3.3) in step 1 is stored as an intermediate product, which may be utilized later by other software modules (e.g. for phase unwrapping).

During the second filtering step, we performed tests with different window sizes and found that relatively large window sizes produced better results with our test data. The results shown in this section were obtained by using an averaging filter with a window size of 33×33 pixels.

Figure 7(*a*) shows the ERS-2 interferometric height errors as a function of the filtered coherence values. The points in the plot were derived after subsampling the original difference DEM from figure 5(*c*) by a factor five in each direction in order to reduce the point cloud density. One can recognize that larger height errors tend to be associated with lower coherence values, which indicates the usefulness of the interferometric coherence as a quality measure for subsequent merging. For comparison, the relationship between the stereoscopic height errors and ERS-2 interferometric coherence is shown in figure 7(*c*). As expected, the two values appear to be highly uncorrelated.

Similar results were obtained from the Radarsat data, as can be recognized from the scatter plots in figure 7(*b*) and (*d*). Figure 7(*b*) shows the Radarsat interferometric height errors as a function of the filtered Radarsat coherence. Similarly to the ERS case, the most prominent errors occur at low coherence values. The relationship between the Radarsat stereo result and the Radarsat interferometric coherence is plotted in figure 7(*d*).

We implemented a fusion algorithm based on computing the weighted average of the stereo and InSAR DEMs. The weights were derived from the filtered coherence map by linearly mapping a suitable subrange (c_1, c_2) of the coherence values into weights between 0 and 1. This means that in regions with a reliable interferometric result, as indicated by coherence values above c_2, the stereo information is completely discarded. On the other hand, in strongly decorrelated areas characterized by values below c_1, the best results were obtained by utilizing only the stereo DEM. Besides the straightforward linear mapping, we performed an additional test in which we chose a quadratic mapping law as a simple example of a higher order mapping function. No significant change of the results was observed.

We derived initial estimates for the merging parameters c_1 and c_2 from the scatter plots in figure 7(*a*)–(*d*). We then optimized the threshold values manually. The ERS-2 and Radarsat merging results shown in figure 7(*e*) and (*f*) were obtained by using $c_1 = 0.34$ and $c_2 = 0.47$. During the manual fine-tuning of the

parameters, we found that a parameter variation Δx of the lower and upper threshold c_1 and c_2, respectively, changed the error mean value and standard deviation of the merged DEMs by less than 1 m, as long as $|\Delta x|$ remained smaller than 0.02.

Besides the interferometric coherence, we also considered using the stereoscopic confidence values, which were derived from the correlation surface of the individual stereo match points (see §3.2), for the merging algorithm. However, we found that some of the major stereoscopic errors in the lower-lying, homogeneous parts of the DEM were not well reflected by the shape of the correlation surface. We therefore abstained from incorporating the stereo-derived estimates into the merging process.

The result of merging the Radarsat stereo with the ERS-2 and Radarsat interferometric DEMs is given in figure 7(*e*) and (*f*), respectively. A visual comparison of these plots to the corresponding plots in figure 7(*a*)–(*d*) confirms that the fusion process successfully substituted the more robust stereo measurements for the most severe interferometric errors. The DEMs obtained by combining the Radarsat stereo with the Radarsat and ERS-2 interferometric DEMs are given in the bottom row of figure 2. The erroneous terrain heights in the upper part of the InSAR DEMs in figure 2(*c*) and (*d*) were replaced by the smoother stereo heights from figure 2(*b*).

The achieved improvement is also visible in the difference DEMs of figure 5(*d*) and (*e*) and the error histograms of figure 6. In the central part of the ERS histogram in figure 6(*a*), the fusion DEM (solid curve) follows the high-quality interferometric reconstruction (dashed curve) and exhibits an even higher peak than the original curve. At the same time, the former interferometric outliers in the histogram wings were suppressed with the use of the Radarsat stereo data (dotted curve). For the Radarsat result shown in figure 6(*b*), the height of the central histogram peak is similar for the InSAR (dashed curve) and merged DEM (solid curve). However, the improvement is clearly visible in the outer regions of the histogram, which are shown in the enlarged view of figure 6(*c*).

The quantitative results obtained from the ERS-2 and Radarsat data are summarized in tables 2 and 3. Table 2 provides a closer look at the cumulative error values in the histogram wings. The table entries focus on error values of 25 m or more, for which the SPOT DEM—despite its limited usefulness for high-precision interferometric evaluation—presents a perfectly valid reference. The listed figures confirm the error suppression achieved by merging.

When comparing the much larger error values of the InSAR reconstruction with the stereo result in table 3, it should be noted that due to the different shapes of the stereo and interferometric error histograms, the error mean and standard deviation

Table 3. Error analysis of reconstructed DEMs.

	Reconstruction error	
DEM	Mean (m)	SD (m)
Stereo	6.4	45.4
InSAR (Radarsat)	17.7	118.9
Merged DEM (Radarsat)	1.6	27.3
InSAR (ERS-2)	27.9	103.6
Merged DEM (ERS-2)	5.3	34.8

do not fully describe the overall quality of the individual reconstructions. However, we can see that in both the ERS-2 and Radarsat case the fusion DEM exhibited a significantly lower error rate than the stereo or corresponding interferometric DEM individually, which demonstrates again the higher accuracy of the merged DEM.

Motivated by the different levels of detail visible in the stereo- and interferometry-derived DEMs, we carried out some further experiments in which we combined low spectral components of the stereo DEM with the high-frequency information of the interferometric DEM. The idea was to apply the spectral merging only to areas with medium or high interferometric coherence in order to avoid the prominent high-frequency interferometric errors that arise at low coherence values, as obvious from figures 5 and 7. In practice, the spectral merging algorithm consisted of two steps. In step 1, we extracted the lower spatial frequencies from the stereo DEM and merged them with the higher-frequency components of the InSAR DEM. The threshold frequency was set manually. In step 2, we employed the correlation-based merging algorithm described above to combine the spectrally merged result from step 1 with the original stereo DEM. In other words, step 2 suppresses the effects of the spectral merging in regions of low coherence. The results of these tests are of comparable quality to those obtained by direct computation of the weighted average, as described above. The increased complexity of the frequency-domain fusion algorithm therefore appears unjustified.

All the fusion experiments described thus far were performed in the DEM geometry. Since vertical height errors in the image geometry result in both a vertical height error and a horizontal displacement after geocoding, we also performed the coherence- and frequency-based merging of the stereo and InSAR heights in the original image geometry, where the erroneous height-induced horizontal shift is not present. We then geocoded the fusion heights and compared them to our reference DEM.

Tests with our Radarsat stereo and interferometric data in the geometry of the std4 image delivered results very similar to the fusion of the geocoded heights; no significant improvement was observed. We found that this effect can be attributed greatly to our particular merging algorithms, which substitute the interferometric heights entirely with the stereo measurements in regions with low coherence. This means that those regions containing the most significant interferometric height errors—along with the largest horizontal displacements—are not affected at all by the merging process; hence, they do not benefit from the potential higher accuracy of the image domain approach.

6. Conclusions and outlook

In our experiments with Radarsat and ERS-2 images of the Asal Rift test site, we found that in areas without technique-related problems, interferometric mapping clearly outperformed the stereo method. However, the relatively long baselines used in our study, in combination with additional decorrelation caused by vegetation, led to some severe phase-unwrapping problems in areas of rough topography; the resulting elevation errors of 200 m or more are obviously not acceptable for practical mapping tasks. These measurements need to be supplemented by height information from other sources.

The generally smoother and lower-quality stereo reconstruction was able to capture the main, low-spatial-frequency terrain structures in most parts of the

image, including the mountainous regions. As opposed to the interferometric result, no obvious outliers are discernible in the stereo error histogram. We have demonstrated that the pronounced interferometric errors arising in steep relief areas can be largely suppressed by combining the interferometric elevation map with the more robust stereo heights. The low-pass-filtered coherence map reflects well the local quality of the InSAR heights and can be utilized in a straightforward way to merge the two DEMs based on weighted averaging. On the other hand, we found that in areas with comparatively small interferometric inaccuracies—up to approximately one phase cycle in our Radarsat imagery—the stereo-derived DEM with its standard deviation of 45 m does not seem to provide sufficiently accurate additional information to improve the InSAR result. We expect this limit to decrease in the future, when higher-resolution SAR images become available from the next generation of SAR sensors (e.g. Radarsat-2).

In our study, we have concentrated primarily on interferometric height errors caused by low coherence and related phase-unwrapping problems. A possible topic for future research would be to investigate the error properties of elevation maps corrupted by other phenomena such as atmospheric artefacts or orbital uncertainties, along with the development of interferometry–stereo fusion techniques that mitigate these errors.

Acknowledgments

The authors wish to thank Scott Hensley from NASA/JPL for providing his matching software. Furthermore, we would like to thank Hannes Raggam from JOANNEUM RESEARCH for his support with the RSG software package and the helpful discussions during the revision of this paper. The ERS-2 and Radarsat data were obtained under the ERS AO3-245 and the ADRO-373 projects, respectively. This study was supported by a Max Kade research grant.

References

AKIMA, H., 1978, A method of bivariate interpolation and smooth surface fitting for irregularly distributed data points. *ACM Transactions on Mathematical Software*, **4**, 148–159.

BAMLER, R., GEUDTNER, D., SCHÄTTLER, B., VACHON, P., STEINBRECHER, U., HOLZNER, J., MITTERMAYER, J., BREIT, H., and MOREIRA, A., 1999, Radarsat ScanSAR interferometry. *Proceedings IGARSS'99, Hamburg, Germany, July 1999* (Piscataway, NJ: IEEE Publications), pp. 1517–1521.

BUCKLEY, S., ROSEN, P., and PERSAUD, P., 2000, ROI_PAC Documentation, Repeat Orbit Interferometry Package. http://topex.ucsd.edu/rs/ROI_PAC_doc.pdf.

CHEN, P., and DOWMAN, I., 1996, Space intersection from ERS-1 synthetic aperture radar images. *Photogrammetric Record*, **15**, 561–573.

CHEN, P., and DOWMAN, I., 2001, A weighted least squares solution for space intersection of spaceborne stereo SAR data. *IEEE Transactions on Geoscience and Remote Sensing*, **39**, 233–240.

CHEN, C., and ZEBKER, H., 2000, Network approaches to two-dimensional phase unwrapping: intractability and two new algorithms. *Journal of the Optical Society of America A*, **17**, 401–414.

CRESSIE, N., 1991, *Statistics for Spatial Data* (New York: John Wiley and Sons).

DOWMAN, I., and CHEN, P., 1998, A rigorous stereo method for DEM generation from Radarsat data. *Radarsat ADRO Symposium, Montreal, Canada, October 1998*, http://www.space.gc.ca/csa_sectors/earth_environment/radarsat/radarsat_info/sup_programs/adro/adroresults/adrocd/papers/ADRO136i.pdf.

FRANKOT, R., SHAFER, S., and HENSLEY, S., 1994, Noise resistant estimation technique for

SAR image registration and stereo mapping. *Proceedings IGARSS'94, Pasadena, CA, August 1994* (Piscataway, NJ: IEEE Publications), pp. 1151–1153.

GOLDSTEIN, R., ZEBKER, H., and WERNER, C., 1988, Satellite radar interferometry: two-dimensional phase unwrapping. *Radio Science*, **23**, 713–720.

GRAHAM, L., 1974, Synthetic interferometer radar for topographic mapping. *Proceedings of the IEEE*, **62**, 763–768.

GÜLCH, E., 1991, Results of test on image matching of ISPRS WG III/4. *ISPRS Journal of Photogrammetry and Remote Sensing*, **46**, 1–8.

HENDERSON, F., and LEWIS, A., 1998, *Manual of Remote Sensing*, Volume 2, *Principles and Applications of Imaging Radar*, 3rd edn (New York: John Wiley & Sons).

KAUPP, V., BRIDGES, L., PISARUCK, M., MACDONALD, H., and WAITE, W., 1983, Simulation of spaceborne stereo radar imagery: experimental results. *IEEE Transactions on Geoscience and Remote Sensing*, **GE-21**, 400–405.

LA PRADE, G., 1963, An analytical and experimental study of stereo for radar. *Photogrammetric Engineering and Remote Sensing*, **35**, 294–300.

LEBERL, F., 1990, *Radargrammetric Image Processing*, 1st edn (Norwood, MA: Artech House).

LEBERL, F., DOMIK, G., RAGGAM, J., CIMINO, J., and KOBRICK, M., 1986, Multi incidence angle SIR-B experiment over Argentina: stereo-radargrammetric analysis. *IEEE Transactions on Geoscience and Remote Sensing*, **GE-24**, 482–491.

LEBERL, F., MAURICE, K., THOMAS, J., and MILLOT, M., 1994, Automated radar image matching experiment. *ISPRS Journal of Photogrammetry and Remote Sensing*, **49**, 19–33.

LIN, Q., VESECKY, J., and ZEBKER, H., 1994, Comparison of elevation derived from INSAR data with DEM over large relief terrain. *International Journal of Remote Sensing*, **15**, 1775–1790.

MASSONET, D., and RABAUTE, T., 1993, Radar interferometry: limits and potential. *IEEE Transactions on Geoscience and Remote Sensing*, **31**, 455–464.

PAILLOU, P., and GELAUTZ, M., 1999, Relief reconstruction from SAR stereo pairs: the 'optimal gradient' matching method. *IEEE Transactions on Geoscience and Remote Sensing*, **37**, 2099–2106.

PRATI, C., and ROCCA, F., 1990, Limits to the resolution of elevation maps from stereo SAR images. *International Journal of Remote Sensing*, **11**, 2215–2235.

RAGGAM, J., and ALMER, A., 1990, Mathematical aspects of multi-sensor stereo mapping. *Proceedings IGARSS'90, Washington, DC, May 1990* (Piscataway, NJ: IEEE Publications), pp. 1963–1966.

RAGGAM, J., and ALMER, A., 1996, Assessment of the potential of JERS-1 for relief mapping using optical and SAR data. *International Archives of Photogrammetry and Remote Sensing, 31-B4, Vienna, Austria, July 1996* (Vienna: Institute of Photogrammetry and Remote Sensing, TU Vienna), pp. 671–676.

RAGGAM, J., STROBL, D., HUMMELBRUNNER, W., and ALMER, A., 1993, Investigation of the stereoscopic potential of ERS-1 SAR data. *Proceedings Fourth International GEOSAR Workshop: Quality and Standards of High-Level SAR Data, Loipersdorf, Austria, May 1993* (Farnham, UK: Earth Observation Sciences Limited), pp. 81–88.

ROGERS, A., and INGALLS, R., 1969, Venus: mapping the surface reflectivity by radar interferometry. *Science*, **165**, 797–799.

RSG, 1993, *Remote Sensing Software Package Graz*, software user manual, 3rd edn, Institute for Digital Image Processing, Joanneum Research, Graz, Austria.

SANSOSTI, E., LANARI, R., FORNARI, G., and FRANCESCHETTI, G., 1999, Digital elevation model generation using ascending and descending ERS-1/ERS-2 tandem data. *International Journal of Remote Sensing*, **20**, 1527–1547.

SCHARROO, R., and VISSER, P., 1998, Precise orbit determination and gravity field improvement for the ERS satellites. *Journal of Geophysical Research*, **103**, 8113–8127.

SRTM 2000, Shuttle Radar Topography Mission (SRTM). http://www.jpl.nasa.gov/srtm.

TOUTIN, T., 1996, Opposite-side ERS-1 SAR stereo mapping over rolling topography. *IEEE Transactions on Geoscience and Remote Sensing*, **34**, 543–549.

TOUTIN, T., 1997, Accuracy assessment of stereo-extracted data from airborne SAR images. *International Journal of Remote Sensing*, **18**, 3693–3707.

TOUTIN, T., 1999, Error tracking of radargrammetric DEM from Radarsat images. *IEEE Transactions on Geoscience and Remote Sensing*, **37**, 2227–2238.

TOUTIN, T., 2000, Evaluation of radargrammetric DEM from Radarsat images in high relief areas. *IEEE Transactions on Geoscience and Remote Sensing*, **38**, 782–789.

TOUTIN, T., and GRAY, L., 2000, State-of-the-art of elevation extraction from satellite SAR data. *ISPRS Journal of Photogrammetry and Remote Sensing*, **55**, 13–33.

ZEBKER, H., and GOLDSTEIN, R., 1986, Topographic mapping from interferometric SAR observations. *Journal of Geophysical Research*, **91**, 4993–4999.

ZEBKER, H., MADSEN, S., MARTIN, J., WHEELER, K., MILLER, T., LOU, Y., ALBERTI, G., VETRELLA, S., and CUCCI, A., 1992, The TOPSAR interferometric radar topographic mapping instrument. *IEEE Transactions on Geoscience and Remote Sensing*, **30**, 933–940.

ZEBKER, H., WERNER, C., ROSEN, P., and HENSLEY, S., 1994, Accuracy of topographic maps derived from ERS-1 interferometric radar. *IEEE Transactions on Geoscience and Remote Sensing*, **32**, 823–836.